

Computer Methods in Biomechanics and Biomedical Engineering: Imaging & Visualization

ISSN: (Print) (Online) Journal homepage: <https://www.tandfonline.com/loi/tciv20>

Optimised CNN based Brain Tumour Detection and 3D Reconstruction

Sushitha Susan Joseph & Aju Dennisan

To cite this article: Sushitha Susan Joseph & Aju Dennisan (2023) Optimised CNN based Brain Tumour Detection and 3D Reconstruction, Computer Methods in Biomechanics and Biomedical Engineering: Imaging & Visualization, 11:3, 796-811, DOI: [10.1080/21681163.2022.2113436](https://doi.org/10.1080/21681163.2022.2113436)

To link to this article:
<https://doi.org/10.1080/21681163.2022.2113436>



Published online: 28 Sep 2022.



Submit your article to this journal



Article views: 89



View related articles



View Crossmark data



Citing articles: 1 View citing articles

Full Terms & Conditions of access and use can be found at
<https://www.tandfonline.com/action/journalInformation?journalCode=tciv20>

Optimised CNN based Brain Tumour Detection and 3D Reconstruction

Sushitha Susan Joseph and Aju Dennisan

School of Computer Science and Engineering, Vellore Institute of Technology, Vellore, India

ABSTRACT

The brain tumour classification and its early identification are significant for treating the tumour efficiently. The 3D visualisation and detection of the brain tumours from MRI is an error-prone task and computationally time-consuming one. This paper offers a 3D reconstruction scheme for reconstruction of brain tumour. Initially, the preprocessing is performed by the process of average filter and histogram equalisation. Subsequently, the K-means clustering-based segmentation is carried out. As a novelty, to detect the brain tumour, an optimised convolutional neural network (CNN) is employed, in which the training process is carried out by a new Levy-adopted Tunicate Swarm Algorithm (L-TSA) through the optimal weight tuning. At last, the 3D reconstruction of brain tumours is performed by the improved marching cube (MC) algorithm for accurate 3D construction of the tumour region. At last, the performance of developed approach is carried out in MATLAB, and the results are verified for the extant schemes concerning certain metrics like sensitivity, FNR, specificity, FPR, accuracy, FNR, precision, MCC, NPV and F1-score. Accordingly, the accuracy of the adopted CNN+L-TSA algorithm attains a higher value of ~0.934 to extant schemes, including CNN +GWO, CNN+EHO, CNN+TSA and CNN+CUGWA, correspondingly.

1. Introduction

Imaging in the medical field is a developed study that has benefited society in a variety of ways during the last few decades (Tang 2016; Shaul et al. 2020; Bisandu et al. 2022). Here, imaging modalities, including CT scan, endoscopy, MRI as well as others, are used in the medical field (Bollero et al. 2019; Germanò et al. 2020; Precenzano et al. 2020; Franco et al. 2020). These imaging modalities are crucial in today's medical operations for the study, diagnosis and treatment of multifactorial disorders (Ghadimi et al. 2018; Khodaei et al. 2018; Akbary et al. 2019; Saeedi et al. 2019; Dehghani et al. 2020). In this field, the image processing techniques like image segmentation and enhancement are required to identify the diagnostic statistics, including the level of severity or detection of disease (Fang et al. 2020; Kumhar et al. 2020). The most recent research area for computer and biomedical scientists is human brain analysis, as it is the main important organ protected by the skull in the human body (Jang et al. 2020). In the human brain, abnormal growth of tissues may cause a brain tumour/anomaly. The tumour in the brain may lead to growth in cells, and they do not die as it is a life-threatening one (Razmjooy, Sheykhammad and Ghadimi 2018; Parsian, Ramezani and Ghadimi 2017). The tumours are classified into two types such as malignant and benign (Duc et al. 2019; Ebner et al. 2019). In addition, the non-cancerous tumour is a benign tumour that is slower in growth, does not spread to its neighbouring normal cells and is small in size; still, the cancerous tumour is a malignant tumour that is fast-growing and larger (Xu, Sheykhammad, Ghadimi and Razmjooy 2020; Zhou et al. 2020b; CONTACT Aju Dennisan daju@vit.ac.in School of Computer Science and Engineering, Vellore Institute of Technology VIT, Vellore, Tamil Nadu 632014, India © 2022 Informa UK Limited, trading as Taylor & Francis Group Cronin et al. 2020).

The enhancement of computational resolution regarding a similar subject in one or more images is known as the SR reconstruction (Han et al. 2018; Hu et al. 2019). Moreover, the SR

ARTICLE HISTORY

Received 1 June 2021

Accepted 9 August 2022

KEYWORDS

Brain tumour; optimal weight; improved marching cube algorithm; 3d reconstruction; CNN reconstruction is encountered in different imaging technologies like photography, medical imaging or video recording and is

extended (Xu, Sheykhammad, Ghadimi and Razmjooy 2020). Even though the reconstruction is more challenging than identification or classification, the 2D visual stimuli reconstruction shows promising outcomes of the activities in the brain (Zhang et al. 2019; Fujita et al. 2019). The 2D artificial images include the handwritten characters, the binary contrast images and the imagery dot patterns. Still, the normal images are highly complex for their reconstruction due to the complex statistical framework (Agus et al. 2018). Therefore, several researchers have reconstructed the difficult normal images and the visual areas via DL models and the anterior visual areas by the Bayesian framework (Sumathi et al. 2018).

The DL-based SR models could remove much data in the LR images for restoring the HR image details (Wei et al. 2019; Lu et al. 2020; Ghosh et al. 2021; Cingireddy et al. 2022). The deep approaches discover the wealthy image features automatically by the hierarchical structure (Lakhellar and Roy 2014; Sharma 2020; Sai Ambati et al. 2020; Afzal 2021; Rustam et al. 2021; Sadiq et al. 2021). Still, it is more difficult to train the deep convolutional neural network (CNN) (Gangappa et al. 2019; Chandanapalli et al. 2019; Rao et al. 2019) effectively due to their vanishing gradient problems. Recently, the researchers proposed 3D CNN models (Vinolin and Vinusha 2018; Shaik and Ganesh 2020) for reconstructing the HR MR images and large numbers of parameters are learned in these approaches. It may cause many challenges in computational expenses like low-resource settings and low cost and memory consumption. In addition, the 3D CNN-

based SR approaches reconstructed many MR slices. The pre-trained CNN approaches (Gokulkumari 2020; Rathod 2020; Gopal 2020) provide superior outcomes for feature extraction as it is a cascade with LSTM and obtained maximum accuracy than the

models like ResNet, AlexNet and GoogleNet (Petersen et al. 2019; Agus et al. 2019). Numerous 3D reconstruction of brain tumour detection models have been presented (Mehmood et al. 2019; Jurek et al. 2019; Du et al. 2020; Mzoughi et al. 2020; Zheng et al. 2020). But, still, common problems exist like complicated imaging models, a need to extend the classification of brain tumours and more memory cost and computation time needs considerable perfection in the segmentation. Hence, there is a need to establish a new framework to provide the issues in the existing models. The main objective is to detect the brain tumour using a new metaheuristic system properly. The contribution of the adopted work is given below:

- Implemented the Levy adopted Tunicate Swarm Algorithm (L-TSA) model for tuning the optimal weights of CNN, ensuring the proper detection of the tumour.
- Introduces an Improved Marching Cube (MC) algorithm for reconstructing the brain tumours in 3D.

The remaining sections includes the following: **Section 2** determines the review on the conventional 3D reconstruction of brain tumour detection models. **Section 3** specifies about the overview of the developed brain tumour detection and 3D reconstruction model. The preprocessing and segmentation of proposed 3D reconstruction model is described in **Section 4**. **Section 5** depicts the tumour detection via optimised CNN: optimal tuning of weights via adopted levy adopted tunicate swarm algorithm. **Section 6** portrays the 3D reconstruction of brain tumours using an improved marching cube algorithm. **Section 7** discussed about the results and discussions. The paper's conclusion is given in **Section 8**.

2. Literature review

2.1. Related works

Mehmood et al. (2019) has developed an intelligent computer-aided diagnostic approach that focuses on the analysis of the human brain using MRI. Moreover, the 3D visualisation system, detection and brain tumour segmentation have provided the level of expertise, geographical location and quality clinical services of medical specialists. The brain MR images were segmented by an adaptive threshold selection and semi-automatic method. Further, the findings of suggested schemes had shown better sensitivity, high accuracy, maximum specificity and increased F-measure to traditional approaches.

Du et al. (2020) has determined a new DCED network for improving the resolution of MRI. The 3D dilated convolutions were exploited as encoders for extracting the HF features. Further, the dilated encoders have captured the large contextual information through the enlarged receptive field with no extra layers or parameters. Next, the features were decoded by the deconvolution operations for alleviating the gridding artefacts and restore. Here, the decoders and encoders were combined into symmetrically associated blocks for improving the flow of information. Each block output was given to the last convolution layer that facilitates for extracting the hierarchical features. The

resultants of adopted scheme has shown high-frequency information and maximum PSNR value, respectively.

Mzoughi et al. (2020) have designed the fully automatic deep multi-scale 3D CNN framework into LGG and HGG for glioma brain tumour classification by the sequence of entire volumetric T1-Gado MRI. The adopted framework merged the global and local contextual information with lower weights based on a deep network and a 3D convolutional layer through the small kernels. The preprocessing technique was proposed based on adaptive contrast enhancement and intensity normalisation of MRI data. Additionally, the data augmentation technique was used to train the deep 3D network. At last, the proposed model attained better outcomes with 92.49% accuracy to extant approaches.

Zheng et al. (2020) have examined the reconstructed 3D visual images through three decoding approaches like contrast-disparity-decoding, contrast-decoding and disparity-decoding schemes. The testing process was performed in these models via the human-viewed 3D contrast images with fMRI data. Moreover, the V1 and V2, i.e. early visual regions, represented the predominant merits in 3D image reconstruction in contrast-decoding approach. Moreover, the regions in dorsal visual such as MT, V7 and V3A attained the main merits for the disparity-decoding method to decode the 3D image disparity. In the end, the findings of the suggested method has revealed maximum prediction accuracy and better decoding performance.

Jurek et al. (2019) have introduced the use of CNN driven through the patches obtained by three images of orthogonal thick-slice to restore the higher resolution isotropic volumes. Further, the different modalities of voxel brain images were used for assessing the efficiency and validity of the post-processing model available using the BrainWeb database. The reconstructed images were indeed of higher visual quality than the acquired images with the CNN. Furthermore, the restored SR volumes were used to estimate the vessel radii. Moreover, it was determined that the vessel radius values of simulated vessel trees were more. Finally, the proposed model showed restore SR images, best quality, and low error than other models.

Umaba et al. (2018) have proposed an anatomic understanding of intraoperative photographs, simulation and 3D reconstruction scheme and disconnecting the subsequent quadrant from the cadaveric brain. In posterior quadrant disconnection, each step was dissected by the formalin-fixed mature cadaveric brain. Moreover, the intraoperative photographs were chosen with temporo-parieto-occipital epilepsy from the 7-year-old girl. The insular cortex was exposed and the Sylvian fissures were dissected. Further, the experimental results of adopted scheme attained decreasing complications and larger seizure outcomes.

Zhou et al. (2020a) has implemented a novel systems for segmenting brain tumours automatically. Initially, the 3D dense connectivity framework was carried out for feature reuse through constructing the backbone. Then, the new feature pyramid component has designed by the 3D atrous convolutional layers and it was added to fuse multi-scale contexts at the last part of the backbone. The 3D deep supervision framework was determined with the network for promoting the training. Moreover, the resultants of adopted approach has provided less dice loss, better

dice similarity coefficient and low weighted CE loss than extant approaches.

Du et al. (2019) has presented a new CNN depending on anisotropic MR image reconstruction model with short and long skip associations for residual learning. Moreover, the adopted scheme alleviated the issues of gradient departure in deep networks and then learned for restoring the HF details of MR images. The adopted network utilised the 3D T1-weighted MR images with its cross-plane self-similarity for reducing memory usage and computational complexity. The adopted network improved the SR of anisotropic MR images with maximum computational efficiency on experimentation on the clinical brain and simulated MR images. Additionally, the simulation outcomes have shown that the adopted approach performed NLM, sparse coding-based algorithm and classical interpolation methods regarding PSNR, intensity profile, small structures and structural similarity image index.

2.2. Review

Table 1 demonstrates the review on the 3D reconstruction of brain tumour detection. At first, the SVM scheme was determined in Mehmoond et al. (2019), which presents high accuracy, better sensitivity, maximum specificity and increased F-measure, however, need to extend the brain tumour classification into subdivisions that ranges from Grade I to Grade IV. DCED networks were exploited in Du et al. (2020) that offer high-frequency information and maximum PSNR value, but the performance of SSIM and NRMSE were not improved in the suggested scheme. Moreover, the 3D CNN scheme was deployed in Mzoughi et al. (2020) that provides high classification accuracy and lower computational complexity.

Nevertheless, the new technique of ‘CapsNet’ was not investigated for MRI brain tumour classification. Likewise, the GLM analysis has determined in Zheng et al. (2020), which presents maximum accuracy and better decoding outcomes. However, some hypothesis-driven approaches like DCM were not used in adopted system. Moreover, CNN scheme was exploited in Jurek et al. (2019) that have restored SR images, best quality and low error; however, more complicated imaging models and reconstruction were not studied using 3D image patches. In addition, the PIPQ model was introduced in Umaba et al. (2018), which offers decreasing complications and better seizure outcomes. However, more complex to evaluate the seizure outcomes of PQD . BN technique was suggested in Zhou et al. (2020a) that offers less dice loss, better dice similarity coefficient and low weighted CE loss. However, this needs considerable improvement in the segmentation of enhancing cores. Finally, the CNN- based anisotropic MR image reconstruction system was introduced in Du et al. (2019) that offers better reconstruction performance, better PSNR and higher accuracy but leads to memory cost and more computation time. These challenges were considered based on 3D reconstruction of brain tumour detection in present work effectively.

Numerous methods have been focused on the 3D reconstruction of brain tumour detection. However, still there exist common problems like more time complexity, complicated

Table 1. Review on the conventional 3D reconstruction of brain tumour detection methods: features and limitations.

Author (citation)	Suggested approaches	Features	Limitations
Mehmoond et al. (2019)	SVM scheme	<ul style="list-style-type: none"> • High accuracy • Larger sensitivity • Maximum specificity • Increased F-measure 	Need to extend the brain tumours classification into sub- division that ranges from Grade I to Grade IV.
Du et al. (2020)	DCED network	<ul style="list-style-type: none"> • High-frequency information • Maximum PSNR value 	The performance of SSIM and NRMSE were not improved in the proposed model.
Mzoughi et al. (2020)	3D CNN model	<ul style="list-style-type: none"> • High classification accuracy • Lower computational complexity 	The new technique of “CapsNet” was not investigated for MRI brain tumour classification.
Zheng et al. (2020)	GLM analysis	<ul style="list-style-type: none"> • Higher prediction accuracy • Better decoding performance 	Some hypothesis- driven methods like DCM were not used in the adopted model.
Jurek et al. (2019)	CNN model	<ul style="list-style-type: none"> • Restore SR images • Best quality • Low error 	More complicated imaging models and reconstruction were not studied using 3D image patches
Umaba et al. (2018)	PIPQ	<ul style="list-style-type: none"> • Decreasing complications • Better seizure outcomes 	• More complex to evaluate the seizure outcomes of PQD itself.
Zhou et al. (2020a)	BN technique	<ul style="list-style-type: none"> • Less dice loss • Better dice similarity coefficient • Low weighted CE loss 	Needs considerable improvement in the segmentation of enhancing cores
Du et al. (2019)	CNN-based anisotropic MR image reconstruction model	<ul style="list-style-type: none"> • Better reconstruction performance • Better PSNR • Higher accuracy 	More memory cost and computation time.

imaging models, high memory cost and so on. Hence, to overcome the above mentioned issues, this work introduces a metaheuristic scheme for tuning the optimal weights of CNN and thereby ensuring the proper detection of the tumour.

3. Overview of proposed brain tumour detection and 3D reconstruction model

This work offers a novel 3D reconstruction and brain tumour detection. Here, the brain tumours detection involves steps like (a) preprocessing, (b) segmentation, (c) brain tumour detection and (d) 3D reconstruction. Initially, the preprocessing is performed by the average filter and histogram equalisation process. Then, the preprocessed output is subjected to segmentation, where K-

means clustering is used. Moreover, for tumour detection, the optimised CNN is utilised, in which the training process is performed through L-TSA for optimal weight tuning of CNN. In addition, the 3D reconstruction of tumours is performed by the improved Marching Cube algorithm. [Figure 1](#) represents the overall framework of the suggested model. The list of symbols is shown in [Table 2](#).

4. Preprocessing and segmentation of proposed 3D reconstruction model

4.1. Preprocessing

Initially, the input brain tumour images are preprocessed by average filter and histogram equalisation.

Average filter: The average filter or mean filter is the linear class windowed filter that smoothens the 2D image. Further, the filter is worked as a low-pass one. The major objective of the average

filter is to take the average across its neighbourhood for any element in the image. The non-linear digital filtering technique is the median filter, which is often used for noise removal from an image. Thus, the preprocessing step would remove the noise for enhancing the outcomes of later processing.

Histogram Equalisation (file:///E:/2021/03%20March%202021/Sushana%20(107615)%20-%20Paper%20/his-t_eq.pdf): It is an approach used to adjust the intensities of image to improve the contrast.

Consider h as the known image indicated as M_c by the matrix of integer pixel intensities M_r , among 0 to F . F indicates the count of intensity values considered as 256. Moreover, N refers to the normalised histogram of h for all possible intensities.

$$\frac{N_n}{N_{total}} \quad (1)$$

Table 2. Overall fitness analysis of the suggested and existing models.

METHODS	MC ALGORITHM (XU ET AL. 2010)	IMPROVED MC ALGORITHM
Testcase1	177728	176218
Testcase2	110909	107729
Testcase3	157740	155251
Testcase4	186372	184156
Testcase5	186091	182736

In Equation (1), $n \in 0; 1 \dots; L - 1$, N_{total} refers to the total number of pixels, and N_n portrays the pixels count with intensity n . In addition, the equalised image G in histogram is given in Equation (2).

$$G_{ij} = \text{floor}(\delta F \cdot 1 + \frac{N_n}{N_{total}}) \quad (2)$$

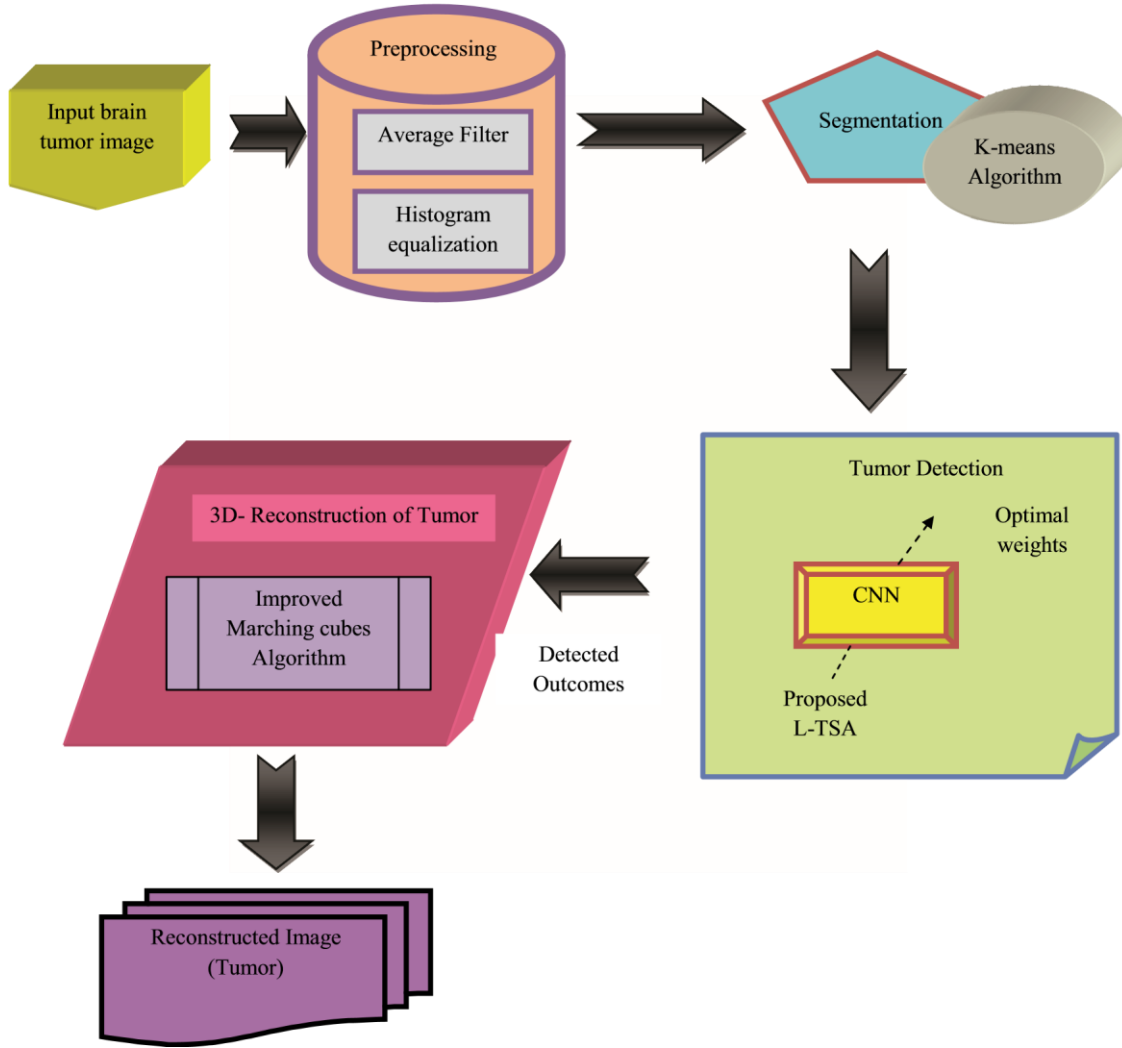


Figure 1. Framework of the suggested work.

List of symbols

Symbols	Description
h	Given image
M_r	Matrix of integer pixel intensities
N	Normalised histogram
Num_{total}	Entire count of pixels
Num_n	Portrays the number of pixels with intensity n
G	Histogram equalised image
k	Transformed pixel intensities
NU	Probability density function
S	Cumulative distributive function
$X_m \delta p$	Distance function of the case m
o	Number of cases
b_i	Denotes the centroid for cluster i
p	Refers to the number of clusters
$Q_{q,y,z}$	Convolutional features
$A \delta p$	Non-linear activation function
$pool \delta p$	Pooling function in each feature maps
${}^q A_{a,y,z}$	Local neighbourhood for every feature map
W_q	Optimal weight vector
B_{qf}	Bias term
L	Total number of weights in CNN
E	Water flow advection in the deep ocean

$\sim R, \delta e p$	Tunicate position
$d_1, d_2, \text{ and } d_3$	Random number ranges among $[0, 1]$
$\sim Z$	Social forces among the search agents
$R_{\max} \text{ and } R_{\min}$	Subordinate and initial speeds for making the social interaction
e	Current iteration
$\sim H$	Food source position
$\sim Y$	Gravity force
$randn$	Random number lies among $[0, 1]$
$\sim D$	Specifies the distance between tunicate and food source
PR	Coordinates of the intersection point
$PR_1 \text{ and } PR_2$	Coordinates of two endpoints
CJ	Isosurface value
$VT_1 \text{ and } VT_2$	Density values of two endpoints
$\Delta x_s, \Delta y_s, \text{ and } \Delta z_s$	Lengths of the cube edges
$DE \delta i r, j r, k r p$	Density at pixel $\delta i r, j r$ in slice $k r$

In Equation (2), $\text{floor}(.)$ integrates the rounds down to its near integer. It is equal to be transformed intensities of pixel k in g through the function.

!

$$S \otimes k \models \forall floor \, \exists F \quad 1 \models_{\substack{n \\ n \neq 0}} N_n \quad (3)$$

For this transformation, the motivation comes from the g intensities and G continuous random variables U, V on \mathbb{R}^2 ; $F 1$ by V is given in Equation (4).

$$V \frac{1}{4} S \delta U p \frac{1}{4} \delta F - 1 p \int_0^{\infty} N U \delta u p du \quad (4)$$

In Equation (4), NU refers to the PDF of g . S indicates the CDF of U multiplied in $\delta F 1\mu$. Let us assume that simplicity S is invertible and differentiable. Moreover, V defines $S \delta U \mu$, which is distributed uniformly on $\% 0; F 1$, in which $NV \delta V \mu \frac{1}{4} F^{-1}_1$.

$$\begin{aligned}
 & \text{---} \quad d \delta_v N V \delta t \delta dt \frac{1}{4} N \delta v \frac{1}{4} N U S \quad \text{---} \quad {}^1 \delta v \delta d \quad {}^1 \delta v \delta d \\
 (6) \quad & dv \quad 0 \qquad \qquad \qquad S \qquad \qquad \qquad dv \\
 & \text{---} \quad \text{---} \quad d \quad {}^1 \delta v \delta \frac{1}{4} \delta d \\
 & v \qquad \qquad \qquad 1 \qquad \qquad \qquad (7) \\
 & \qquad \qquad \qquad S S \qquad \qquad \qquad dv \\
 & \qquad \qquad \qquad dv \qquad \qquad \qquad dv
 \end{aligned}$$

$$\frac{dS}{du} \propto S^{\frac{1}{4}} \delta v \propto \frac{dS}{d\delta v} S^{\frac{1}{4}} \delta F \propto 1 \propto S^{\frac{1}{4}} \delta v \propto \frac{dS}{d\delta v} S^{\frac{1}{4}} \delta F$$

$\frac{1}{4}$

(8)

where $NV\delta vP \frac{1}{4} F^{-1}_1$.

The discrete histogram is an approximation of $NU\delta\bar{u}\bar{b}$, and the transformation in Equation (1) approximates to Equation (2). While the discrete version does not produce the exact flat histograms, it flattens them to improve the image contrast.

4.2. K-Means clustering

The procedure of digital image separation into numerous distinct regions is known as image segmentation which includes each pixel with similar attributes. A pixel set is called as superpixels. Moreover, the image segmentation is used for objects, the boundaries and location like curves and lines in pictures. Further, image segmentation is assigned in the label in an image to each

pixel in which the pixels with similar label distribute some features. The most popular approach, the K-means clustering method (<https://www.kdnuggets.com/2019/08/introduction-image-segmentation-k-means-clustering.html>), is determined for segmentating the tumour in brain. It is an unsupervised algorithm used for segmenting

a particular area from its background. Further, it partitions or clusters the given data into K-clusters based on its K-centroids.

The K-means algorithm is used for unlabelled data (i.e.), data without defining the groups or categories. It finds certain groups based on certain kinds of data similarity with the number of groups as K. The main objective of K-means clustering is to reduce the cluster centre and the sum of squared distances among all points. The function J is defined in Equation (9).

$$X^p X_o \quad \quad \quad 2 \\ J \not\sim \frac{1}{4} \quad \quad \quad Xm\delta l p \quad \quad bI \quad \quad \quad (9) \\ \not\sim \frac{1}{4} m \not\sim \frac{1}{4}$$

In Equation (9), $x_m^{\delta l p}$ indicates the distance function of the case m , o portrays the number of cases, b_l denotes the centroid for cluster l and p refers to the number of clusters. Further, the steps in the K-means model is given below. **Step 1:** Select the number of clusters K .

Step 2: Choose at random points K and the centroid.

Step 3: Allocate every data point to the nearest centroid which formed the K clusters.

Step 4: Calculate and locate the novel centroid of each cluster.

Step 5: Relocate each data point to the novel nearby centroid. If any relocation occurs, go to step 4, else, the model is set.

5.1 Optimised CNN model

The segmented images are subjected to optimised CNN (LeCun et al. 2010) as its input. Moreover, the CNN classifier consists of three layers: convolution, pooling and fully connected layers. In addition, several convolution kernels are present in the convolution layer. Therefore, the complete feature map was developed through certain kernels. In addition, the q^{th} layers corresponding to z^{th} feature map and the feature values in the position $\delta_a; y\beta$ is portrayed as $Q^q_{a,y,z}$ in Equation (10). Similarly, the z^{th} filter value is offered in the q^{th} layer. The bias term and optimal weight vector are determined as B^q_f and W^q_f , respectively. Therefore, the optimal weight tuning is done via adopted L-TSA scheme. Further, the associated input patches in the z^{th} layer at the position $\delta_a ; y\beta$ are given using $C^q_{a,y}$. The non-linearity is obtained through the activation function that assists to predict the multi-layer networks non-linear features. Assume the non-linear activation function as $A \delta\beta$, the convolutional qq features as $Q_{a,y,z}$, and the activation value $A_{a,y,z}$ is determined in Equation (10) and Equation (11). However, in the pooling layer, the shift-variance is established via reducing the resolution of feature

maps as determined in Equation (12). In each feature map, the pooling function are portrayed as pool $\partial\mathbf{p}$, and

q the local neighbour $A_{a,y,z}$ for every feature map at a nearby position $\partial a ; y\mathbf{p}$ is specified as $I_{a,y}$.

$$Q_{qa,y,z} \nabla W_{qf} Tr C_{aq,y} \mathbf{p} B_{qf} \quad (10)$$

$$A_{qa,y,z} \nabla A \quad Q_{qa,y,z} \quad (11)$$

$$O_{qa,y,z} \nabla \text{pool} \quad A_{qa,y,z}; " \partial CS; cr \mathbf{p} 2 I_{a,y} \quad (12)$$

In CNN, the loss function is determined in Equation (13). The CNN constraints $\partial\varphi\mathbf{p}$ are linked with necessary IO input–output

relation is determined as $UT^{\partial sr\mathbf{p}}; VT^{\partial sr\mathbf{p}} \quad ; sr 2 \frac{1}{2}1; IO$.

In addition, the CNN output, sr^{th} input data and the associated target values are given as $OUT^{\partial sr\mathbf{p}}$, $UT^{\partial sr\mathbf{p}}$ and $VT^{\partial sr\mathbf{p}}$, correspondingly.

$$\text{Loss} \nabla \text{_____} 1 X_{ms} P\varphi; VT^{\partial sr\mathbf{p}}; OUT^{\partial sr\mathbf{p}} \quad (13)$$

$$\text{Num } sr \nabla 1$$

The pooling layer in CNN conducts downsampling procedures on the results obtained from the convolutional layers. Furthermore, there are two well-known pooling categories: maximum pooling and average pooling. The greater value is observed in max-pooling, while the average value is observed in average pooling.

It functions within the compressed inputs as a fully linked layer. Generally, the pooling layer's results are fed into the fully connected layer's input, and so the inputs are connected to all layers. The fully connected layer appears at the edges of the CNN model.

5.2. Solution encoding and objective function

Moreover, the CNN weights are tuned optimally using the proposed L-TSA method. Figure 2 illustrates the input solution to the proposed L-TSA scheme. Here, the CNN weight count is indicated as L . The objective function of the implemented method is determined in Equation (14), in which Loss is given in Equation (13).

$$\text{Obj} \nabla \min \partial \text{Loss} \mathbf{p} \quad (14)$$

5.3. Proposed L-TSA model

Even though the conventional TSA (Kaur et al. 2020) model can identify the food source location present in the sea, whereas, it has no thought regarding the food source obtained in search space. To tackle this scenario, the L-TSA model is executed. Normally, self-enhancement is establish to be capable in the existing optimisation models (Rajakumar and George 2012; Rajakumar 2013a, 2013b; Swamy et al. 2013; George and

Rajakumar 2013). In TSA, the two tunicate behaviours are employed to identify the food source. Moreover, the two behaviours of TSA include swarm intelligence and jet propulsion.

Behaviour of Jet propulsion: Here, a tunicate must convince the three circumstances such as remaining near the most excellent search agent, moving towards the location of the most excellent search agent and avoiding search agent conflicts. However, the behaviour of swarm updated another search agent's position depending on the most excellent optimal solution. Further, three conditions of the jet propulsion behaviour are given as follows.

(i) *Avoid the conflicts between search agents:* For avoiding the conflicts among the search agents, the \tilde{X} vector is employed to calculate the new search agent's position, and it is determined in Equation (15).

$$\begin{aligned} \tilde{X} &\nabla \tilde{Y}_- \\ &\tilde{Z} \end{aligned} \quad (15)$$

Where,

$$\tilde{Y} \nabla d_2 \mathbf{p} d_3 \quad \tilde{E} \quad (16)$$

$$\tilde{E} \nabla 2:d_1 \quad (17)$$

In Equation (16) and Equation (17), \tilde{E} represents the water flow advection, \tilde{Y} denotes the gravity force and the variables d_1,d_2 and d_3 indicates the random number in $[0, 1]$. \tilde{Z} indicates the social forces among the search agents given in Equation (18).

$$\tilde{Z} \nabla \frac{1}{4} \nabla R_{\min} \mathbf{p} d_1:R_{\max} \quad R_{\min} \quad (18)$$



Figure 2. Solution encoding.

In Equation (18), R_{\max} and R_{\min} portrays the subordinate and initial speeds for making the social communication. Moreover, R_{\min} is 1 and R_{\max} is 4, correspondingly.

(ii) *Movement to the best neighbour's direction:* Here, the search agents moved to the best neighbour's direction once the conflict was avoided among the neighbours.

$$\tilde{D} \nabla \tilde{H} \quad \text{randn}: \tilde{R}_{\text{seep}} \quad (19)$$

In Equation (19), \tilde{D} specifies the distance among the tunicate and food source (i.e.), search agent, e denotes the current iteration, \tilde{H} refers to food source position, the vector \tilde{R}_{seep} portrays the tunicate position and randn indicates the random number that lies among $[0, 1]$.

(iii) *Proposed Converge to the best search agent:* Conventionally, the search agent could maintain the positions to the food source, i.e. best search agent. Still, as per the suggested L-TSA approach, the location update with levy update is determined in Equation (20).

8

$$\begin{aligned} & \sim H \text{ } \sim x \\ & \sim R_s \delta e p^0 \% >> > \sim R H \delta e p \sim X p: \sim H \sim H \sigma \\ & \text{randrandLevy: } \sim : R \delta \sim R \theta_{ss} \delta p \delta e; e p p; i f i f i J P J P J P = \max = \max \max I T I T I T < \\ & >> \text{randrandrand\&\&randrand} < 00::55 \end{aligned} \quad (20)$$

In Equation (20), $\sim R_s \delta e p^0$ denotes the position update of tunicate based on $\sim H$ food source position.

Swarm behaviour: For simulating the swarm behaviour of tunicate, it saves the first two optimal best solutions, and the other search agent's locations are updated depending on most excellent search agent's position. Moreover, the swarm behaviour of the tunicate is determined in Equation (21).

$$\begin{aligned} & \sim R_s \delta e p \sim 1 p \sim R_s \delta e p \sim R_s \delta e p \\ & \sim 1 p \quad (21) \quad 2 p d_1 \end{aligned}$$

The final position is in a random place within a cone-shaped or cylindrical that describes the tunicate position. Algorithm 1 describes the pseudo-code of the adopted L-TSA model.

Algorithm 1: Pseudo-code of Suggested L-TSA scheme

- Step 1:** Initialization of tunicate population $\sim R_s$.
- Step 2:** Select the total number of iterations and initial parameters.
- Step 3:** The fitness value is computed for each search agent.
- Step 4:** The best search agent is discovered after calculating the fitness value.
- Step 5:** Each search agent's position is updated as per Equation (21).
- Step 6:** The updated search agent has attuned away from the boundary in a specified search space.
- Step 7:** The fitness value is calculated.
- Update $\sim R_s$ only if there is a better solution than the preceding optimal solution.
- Step 8:** The algorithm ends only if the stopping criterion is fulfilled.
Else, repeat the steps from 5–8.

Step 9: The best optimal solution is returned so far.
from the 2 neighbouring slices. Moreover, the MC model would split the field of 3D data into cubes, it ensures the cubes one by one and selects the cubes which interconnect through the isosurface. Next, the intersection points are examined via linear interpolation. At last, the intersection points are connected in the

correct order for obtaining the surface considered the isosurface approximation. Here, an improved MC algorithm is used.

Establish the cubes with the isosurface: The MC model used the implied isosurface extraction technique as it cannot compute the function directly, i.e., $f(x, y, z)$. Moreover, the isosurface is extracted directly from the 3D data field. Assign it to a cube's vertex for finding the isosurface intersection in a cube, only if the data value is larger at that vertex than the CJ isosurface value. Further, these vertices are present within the surface. The vertices less than the isosurface value CJ would obtain 0 at the surface outside. Moreover, it is observed clearly that not every cube holds the isosurface. The outside vertex and inside vertex present in the cubes contain the isosurface.

Since, each of them has two states of outside or inside the isosurface and every cube has 8 vertices; as it has at least $2^8 / 4 = 256$ mesh method in isosurface. Due to inversion and rotational symmetry, the total count in mesh method is lowered to 15.

Figure 3 illustrates the logical cube formation.

Calculation of the normal and coordinates of the intersection: Moreover, the linear interpolation model would determine the intersection point coordinates. The linear interpolation model is determined in Equation (22).

$$\frac{PR \% PR_1 \delta}{PR_1 \delta} \frac{CJ}{VT_1 \delta PR_2} \quad (22)$$

$$\frac{PR \% PR_1 \delta}{PR_1 \delta} \frac{CJ}{VT_2 \delta VT_1 \delta}$$

In Equation (22), PR determines the intersection point coordinates, VT_1 and VT_2 specifies the density values of two endpoints, PR_1 and PR_2 refers to the coordinates of two endpoints and CJ portrays the isosurface value.

In the cube vertex, the normal is calculated through the central difference approach and then the usage of linear interpolation provides the normal at the vertices of the triangle. Further, the central difference is given in Equations (23)–(25). $GL_x \delta ir; jr; kr \% \frac{1}{2} DE \delta ir \sim 1; jr; kr \delta DE \delta ir \sim 1; jr; kr \delta = 2 \Delta x s$ (23)

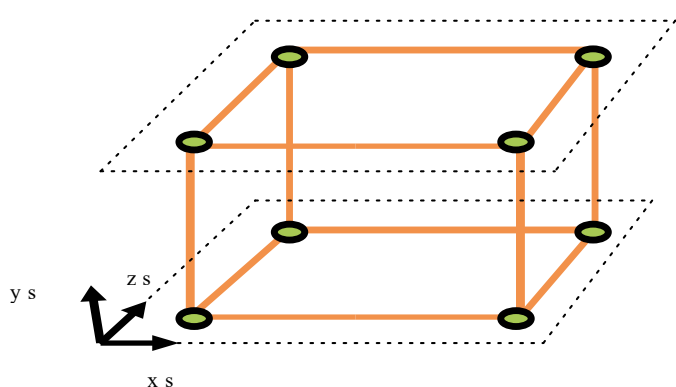


Figure 3. Formation of a logical cube.

$$GL_y \delta ir; jr; kr \% \frac{1}{2} DE \delta ir; jr \sim 1; kr \delta DE \delta ir; jr \sim 1; kr \delta = 2 \Delta y s \quad (24)$$

¹ . 3D reconstruction of brain tumour using improved marching cube algorithm

MCs used the divide-and-conquer model for locating the logical cube's surface that was produced from the 8 pixels, i.e., 4

$$GL_{zs}\partial ir; jr; kr \models \frac{1}{4} \frac{1}{2} DE\partial ir; jr; kr \models 1\models DE\partial ir; jr; kr \quad 1\models=2\Delta z s \quad (25)$$

where Δx_s , Δy_s and Δz_s refers to the lengths of the cube edges, and $DEðir; jr; kr\rho$ indicates the density at the pixel $ðir; jr\rho$ in the slice kr .

MC algorithm's flaws: Even though the implementation of MC algorithms is easy and obtains higher-resolution images. Still, it contains a certain aspect of limitation.

- (i) *Topological inconsistencies result in ambiguity face:* Several ways are used for solving the ambiguity surface that includes the asymptotic decider, gradient convergence criteria, the sub lookup table configuration and the average ambiguity determination approach.
 - (ii) *Lower computing efficiency:* Moreover, the MC algorithm is a series of recognition in each cube that are similar to the complete approach. Here, more information obtained among the neighbouring cubes consists of the frequent computation. A large number of triangular patches are generated (i.e.), which seriously affects the user's interaction up to certain millions of triangle patches.

Improved MC algorithm: There are certain improvements made in the MC algorithm based on the demerits of existing MC algorithms.

(1) *Replacing the cube edge linear interpolation using the selection of midpoint:* The thickness of CT slices is increased slightly as it increases the high-resolution of medical images. Thus, the cube edge's centre point is regarded as the intersection point for computing it via the linear interpolation that makes no dissimilarity in reconstruction outcomes. The triangular patches are created at the time such a way it forms a smoother isosurface in the local area that helps in simplifying the mesh. Moreover, the proposed linear interpolation on Plane is Equation (26). Consider the isovalue as 0. The value is present inside or outside while comparing them to the isovalue and corresponds to the particular list of edges. As per the improved algorithm, the coordinates of endpoints are evaluated as per Equation (27).

$$PR \frac{1}{4} PR_1 \text{p} \xrightarrow{\quad VT_1 \quad} \text{p} \delta PR_2$$

$PR_1 \text{p}$

where

$$PR_1 \frac{1}{4} \text{_____}_1 \pitchfork PR_2 \quad (27)$$

(2) *Contract edge for minimising the triangular patches count:* Moreover, the grid scheme is simplified into four methods like vertex merging, decimation, adaptive subdivision and sampling. The edge contraction method is chosen by merging the simplicity and robustness of the vertex. The three constraint conditions are satisfied only, the edge including the two contract vertices into a point and two vertices merged into one. In addition, the triangle will be kept only when the conditions are not met.

(3) *Proposed distance constraint:* Assume the geometric distance of VT_{ir} and VT_{jr} as $dt \sqrt{VT_{ir} \cdot VT_{jr}}$. Based on this, the MDC is set, and the formulation is given in Equation. (28)

$$dt \; VT_{ir}; \; VT_{jr} \; MDC \quad (28)$$

7. Results and discussion

7.1. *Simulation procedure*

The developed brain tumour detection and reconstruction scheme was implemented in MATLAB, and its resultants are verified. Moreover, the implementation was carried out using the **BRATS** dataset. The original MC images and the improved MC images are demonstrated in [Figure 4](#). Similarly, the identified tumour regions for all five test cases are represented in [Figures 5–9](#). Moreover, the outcomes of the suggested CNN + L-TSA scheme was analysed to the existing approaches including CNN + GWO ([Mirjalili et al. 2014](#)), CNN +EHO ([Wang Wang et al. 2015](#)), CNN +TSA ([Kaur et al. 2020](#)) and CNN+CUGWA ([Joseph 2021](#)), correspondingly. In addition, the outcomes were determined via altering the learning rate as 60, 65, 70, 75, 80, 85 and 90 based on various metrics including accuracy, MCC, F1-score, sensitivity, FPR, precision, NPV, specificity, FNR and FDR, correspondingly.

7.2. Performance analysis

The analysis of adopted CNN+L-TSA scheme is evaluated to existing schemes such as CNN+GWO, CNN+EHO, CNN+TSA and CNN+CUGWA, correspondingly, with respect to various measures and is given in [Figures 10–12](#). Furthermore, the positive metrics such as precision, specificity, accuracy and sensitivity of adopted CNN+L-TSA scheme show better outcomes than other extant scheme as represented in [Figure 10](#). In addition, the accuracy of the suggested CNN+L-TSA scheme as given in [Figure 10\(c\)](#) holds higher values (~ 0.934) for learning percentage 90; still, the extant scheme holds the least values. Likewise, the suggested CNN+MSGWA model attains higher sensitivity for learning percentage 60; and it is 1.01%, 0.56%, 0.44% and 0.22% superior to the traditional schemes such as CNN+GWO, CNN+EHO, CNN+TSA and CNN +CUGWA, correspondingly in [Figure 10\(d\)](#). Moreover, the adopted CNN+L-TSA model holds maximum specificity (~ 0.923) for learning percentage 80 to extant schemes in [Figure 10\(b\)](#). The adopted CNN+L-TSA scheme holds maximum precision outcomes (~ 0.922) in [Figure 4\(a\)](#) when compared to the existing schemes such as CNN+GWO (~ 0.907), CNN+EHO (~ 0.905), CNN+TSA (~ 0.912) and CNN+CUGWA (~ 0.91), correspondingly, for learning percentage 80. Therefore, the betterment of suggested CNN+MSGWA scheme is attained capably for detection and 3D reconstruction of brain tumour detection.

The negative measures analysis of the suggested CNN +MSGWA model to conventional schemes is illustrated in Figure 11. Further, the negative measures such as FDR, FNR and FPR should be minimal for obtaining superior outcomes. In



Test case 1		
Test case 2		
		A red 3D surface model of a brain, oriented laterally.
		A red 3D surface model of a brain, oriented laterally.
		A red 3D surface model of a brain, oriented laterally.
		A red 3D surface model of a brain, oriented laterally.
Test case 3		
Test case 4		

Test case 5		
	(a)	(b)

Figure 4. Reconstructed 3D brain MRI images: (a) orginal MC image (b) improved MC image.

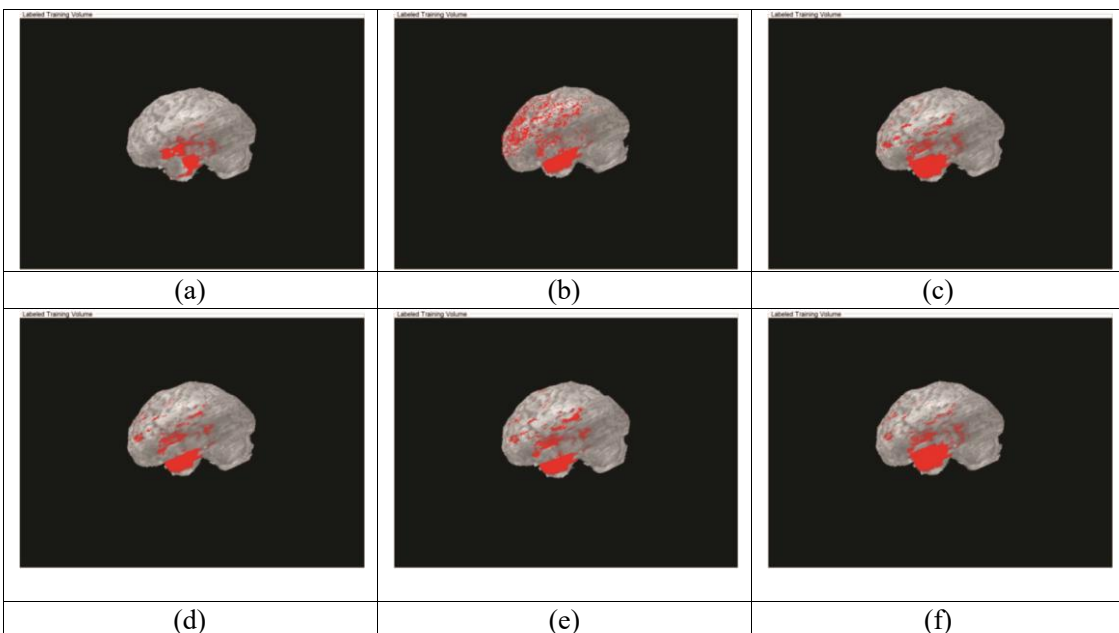


Figure 5. Identified tumour region for test case 1: (a) orginal image, (b) EHO, (c) CUGWA, (d) GWO, (e) TSA and (f) proposed L-TSA.

Figure 6. Identified tumour region for Test case 2: (a) orginal image, (b) EHO, (c) CUGWA, (d) GWO, (e) TSA and (f) proposed L-TSA.

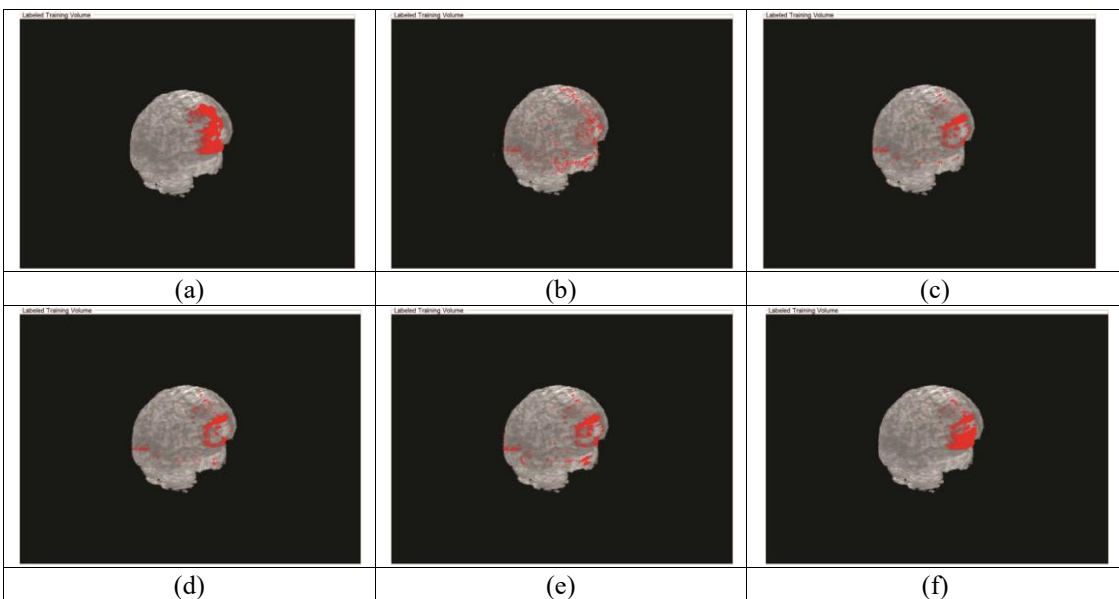
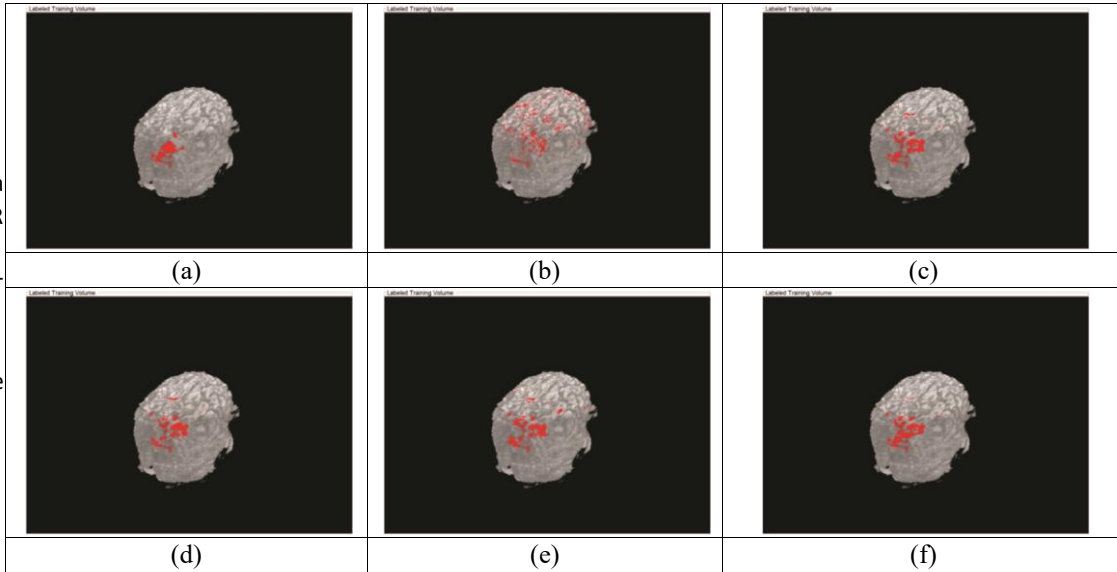


Figure 7. Identified tumour region for Test case 3: (a) orginal image, (b) EHO, (c) CUGWA, (d) GWO, (e) TSA and (f) proposed L-TSA.

addition, the adopted CNN+L-TSA model attains a lower FPR value (~ 0.069) for learning percentage 90 but the existing schemes like CNN+GWO (~ 0.077), CNN+TSA



(~ 0.075) and CNN +CUGWO (~ 0.073), respectively, in Figure 11(a).

The adopted CNN+L-TSA model for learning percentage 80 achieves better outcomes (~ 0.075) with least FDR values to traditional approaches in Figure 11(c). Likewise, the FNR of the suggested CNN+L-TSA model for learning percentage 70 is 3.09%, 4.123%, 8.24% and 13.10% better than the other conventional schemes including CNN+GWO, CNN+EHO, CNN+TSA and CNN+CUGWA, respectively, in Figure 11(b). Thus, the improvement of the adopted CNN+L-TSA model is proved.

Figure 12 illustrates the other measures analysis of the suggested and traditional schemes. The suggested CNN +L-TSA scheme holds NPV values (~ 0.922) to extant methods for learning percentage 80 in Figure 12(a). In addition, the suggested CNN+L-TSA scheme has larger MCC values at learning percentage 60, that is 0.906% and 1.55% to extant methods like CNN+CUGWA, and CNN+GWO, correspondingly, in Figure 12(c). The suggested CNN+L-TSA scheme obtains higher value (~ 0.923), while the extant schemes including CNN+GWO (0.91), CNN+EHO ($\sim 0.0.916$), CNN+TSA (~ 0.914) and CNN +CUGWA (~ 0.909) achieve minimum values for learning percentage 80 in Figure 11(b). This proves the outcomes of the suggested scheme is better in detecting the brain tumour based on 3D reconstruction. Still, the existing schemes show their poor performance in detecting brain tumours with poor detection outcomes.

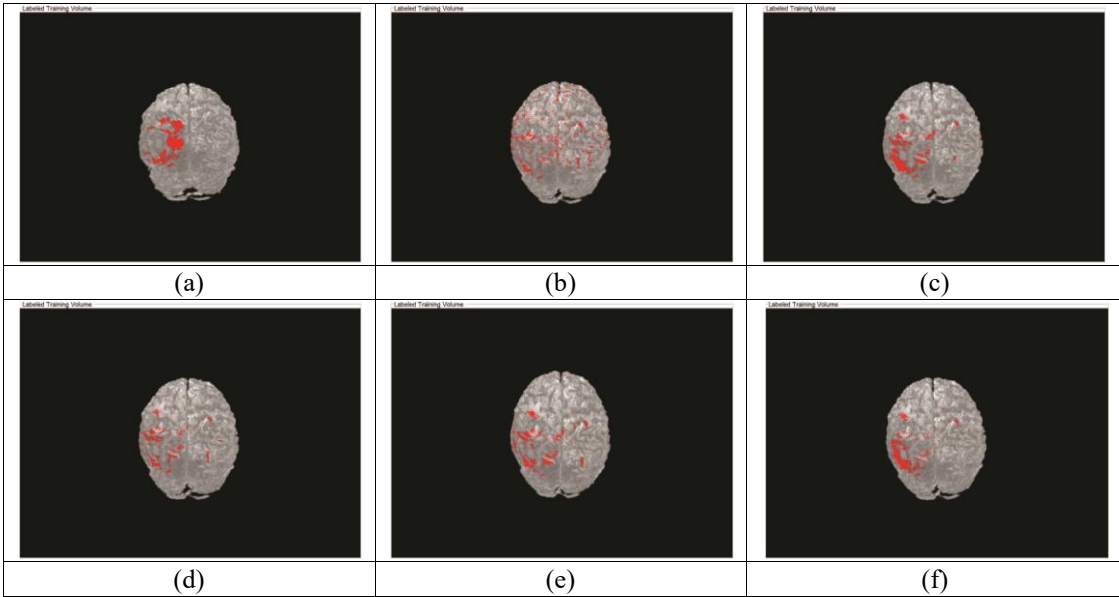


Figure 8. Identified tumour region for Test case 4: (a) orginal image, (b) EHO, (c) CUGWA, (d) GWO, (e) TSA and (f) Proposed L-TSA.

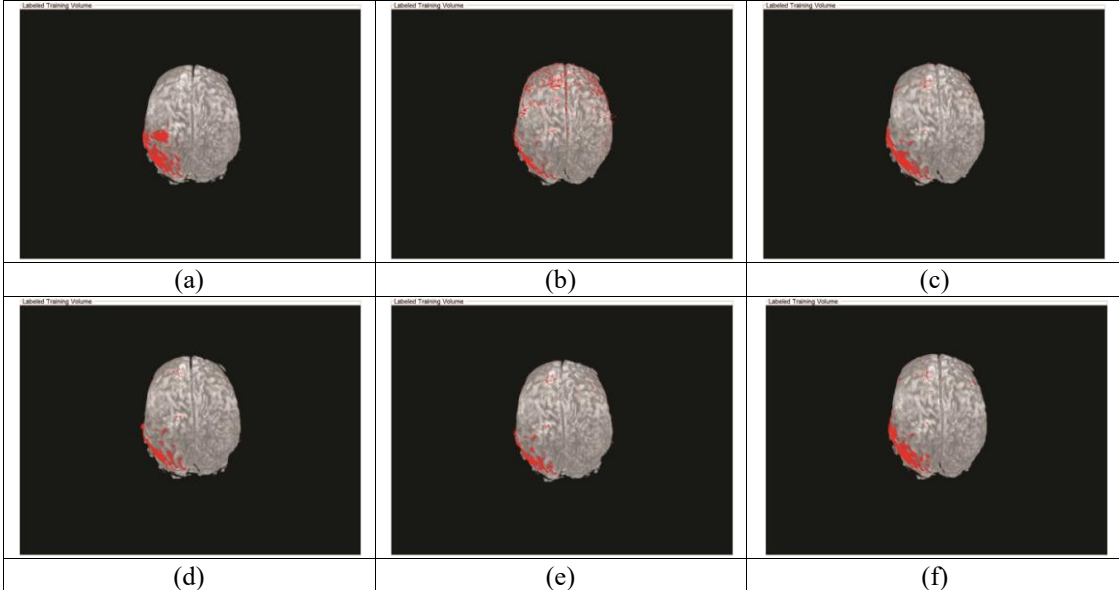


Figure 9. Identified tumour region for Test case 5: (a) orginal image, (b) EHO, (c) CUGWA, (d) GWO, (e) TSA and (f) proposed L-TSA.

7.3. Analysis on vertices

Table 2 describes the analysis based on vertices of the improved MC algorithm over other existing MC (Xu et al. 2010) algorithms. The table clearly shows that the vertices of the improved MC algorithm show lower values with better outcomes than other traditional MC algorithms. For test case 5, the improved MC algorithm holds a minimum value (182736) than other traditional MC algorithms.

7.4. Statistical analysis

The statistical analysis of the suggested CNN+L-TSA scheme than other existing schemes based on Bookmaker Informedness (BM),

False Omission Rate (FOR) and Markedness (MK) measures is illustrated in Tables 3–5. Moreover, the proposed CNN+L-TSA method shows superior outcomes with the lowest FOR values (0.11531) to extant schemes such as CNN+GWO, CNN+EHO, CNN+TSA and CNN +CUGWO, correspondingly, under a worst-case scenario in Table 3. The adopted CNN+L-TSA scheme holds a higher BM value (0.86536) to existing schemes under the best-case scenario in Table 4. The proposed CNN+L-TSA method in Table 5 obtains the MK value of 0.82075 for the mean case scenario, which is superior to extant schemes. From the outcome, it is evident that the proposed Levy adopted Tunicate Swarm Algorithm (L-TSA) optimisation algorithm

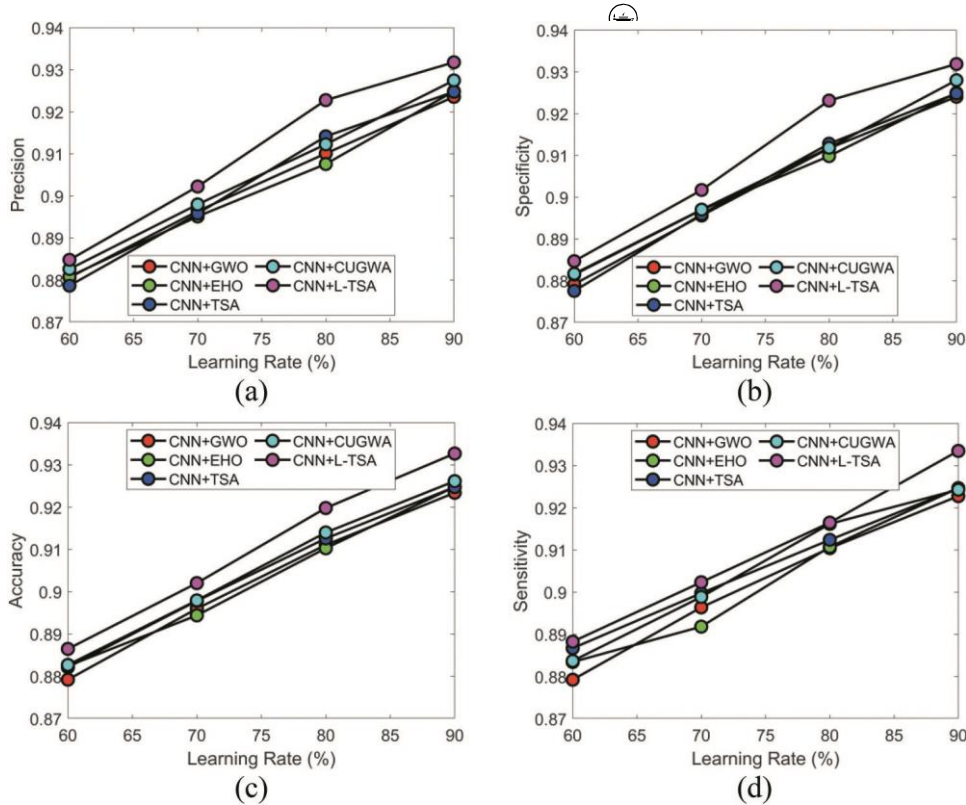


Figure 10. Performance analysis of the suggested CNN+L-TSA scheme to extant approaches for (a) precision, (b) specificity, (c) accuracy and (d) sensitivity.

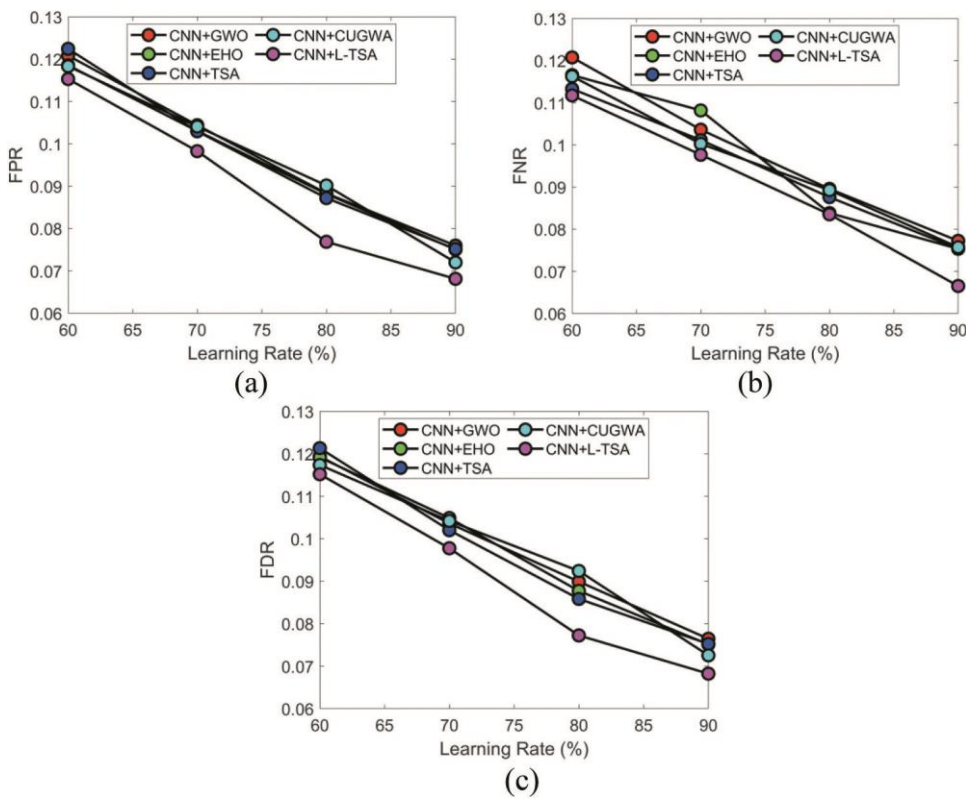


Figure 11. Performance analysis of the suggested CNN+L-TSA scheme to extant approaches for (a) FPR, (b) FNR and (c) FDR.

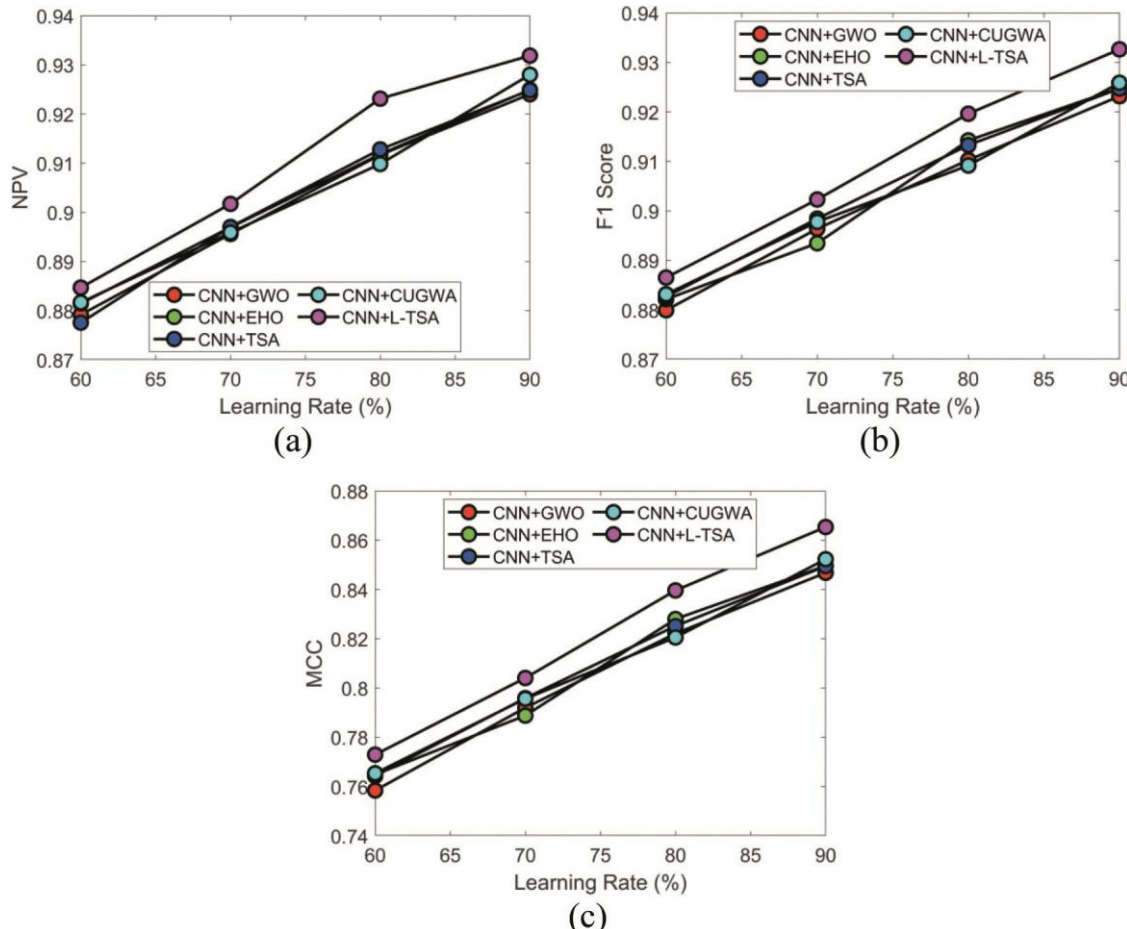


Figure 12. Performance analysis of the suggested CNN+L-TSA scheme to extant approaches for (a) NPV, (b) F1-score and (c) MCC.

Table 3. Statistical analysis of the adopted CNN+L-TSA scheme to other extant models for FOR.

Methods	CNN+GWO (MIRJALILI ET AL. 2014)	CNN+EHO (WANG WANG ET AL. 2015)	CNN+TSA (KAUR ET AL. 2020)	CNN+CUGWA (JOSEPH SS)	PROPOSED CNN+L-TSA
Mean	0.097373	0.096202	0.096938	0.096144	0.089643
Worst	0.12082	0.11854	0.12244	0.11832	0.11531
Best	0.075968	0.075046	0.075159	0.071994	0.068121
STD	0.01949	0.018778	0.02046	0.019783	0.021289
Median	0.096351	0.09561	0.095079	0.097128	0.087571

Table 4. Statistical analysis of the proposed CNN+L-TSA model over other existing models for BM.

Methods	CNN+GWO (MIRJALILI ET AL. 2014)	CNN+EHO (WANG WANG ET AL. 2015)	CNN+TSA (KAUR ET AL. 2020)	CNN+CUGWA (JOSEPH SS)	PROPOSED CNN+L-TSA
Worst	0.75842	0.7649	0.76428	0.76537	0.77295
STD	0.038207	0.038114	0.036846	0.036912	0.040447
Median	0.80706	0.80839	0.81054	0.80812	0.82184
Mean	0.80484	0.80782	0.80871	0.80847	0.8205
Best	0.8468	0.84961	0.84949	0.85229	0.86536

Table 5. Statistical analysis of the proposed CNN+L-TSA model over other existing models for AK.

Methods	CNN+GWO (MIRJALILI ET AL. 2014)	CNN+EHO (WANG WANG ET AL. 2015)	CNN+TSA (KAUR ET AL. 2020)	CNN+CUGWA (JOSEPH SS)	PROPOSED CNN+L-TSA
Median	0.80689	0.80809	0.81099	0.80457	0.82494
STD	0.03789	0.038066	0.040554	0.03879	0.042357



Mean	0.8053	0.80708	0.80696	0.80723	0.82075
Worst	0.75981	0.76231	0.75624	0.7643	0.76949
Best	0.84759	0.84984	0.8496	0.85546	0.86365

helps in providing a better detection rate. Further, an accurate 3D tumour region is attained using the improved Marching Cube (MC) algorithm.

8. Conclusion

This paper introduced a 3D reconstruction model for brain tumour reconstruction. Here, an optimised CNN was used for brain tumour detection, where a new L-TSA algorithm carried out the training process via tuning the optimal weight. Finally, the 3D reconstruction of brain tumours was performed by the improved Marching Cube (MC) algorithm for accurate 3D construction of the tumour region. Further, the outcomes of the suggested scheme was calculated to the extant methods under certain metrics. On observing the graph, the accuracy of the proposed CNN+L-TSA method attained better values (~0.934) than the traditional methods. This proves the betterment of adopted work tumour detection with a better detection rate. Furthermore, the results also show the effect of optimal training of the model as it could enhance the detection accuracy in a precise manner.

Nomenclature

BM	Bookmaker Informedness	NRMSE	Normalized Root Mean Squared Error
BoW	Bag of Words	NLM	Non-Local Means
BN	Batch normalization	CDF	Cumulative Distributive Function
CE	Cross-Entropy	PQD	Posterior Quadrant Disconnection
CT	Computed Tomography	PSNR	Peak Signal to Noise Ratio
FOR	False Omission Rate	PIPQ	Peri-Insular Posterior Quadrantectomy
CapsNet	Capsule Networks	SSIM	Structural Similarity Image Metric
CNN	Convolutional Neural Networks	SR	Super Resolution
FDR	False Discovery Rate	MRI	Magnetic Resonance Imaging
DCM	Dynamic Casual Model	PDF	Probability Distributive Function
DCED	Dilated Convolutional Encoder-Decoder	3D	Three-Dimensional
DL	Deep Learning	2D	Two-Dimensional
DICOM	Digital Imaging And Communications in Medicine		
FMRI	Functional Magnetic Resonance Imaging		
FNR	False Negative Rate		
FPR	False positive rate		
FLAIR	Fluid-Attenuated Inversion Recovery		
GLM	Generalized Linear Model		
HR	High Resolution		
HF	High-Frequency		
HGG	High-Grade Glioma		
LSTM	Long Short-Term Memory		
LGG	Low-Grade Gliomas		
MCC	Matthews Correlation Coefficient		
L-TSA	Levy adopted Tunicate Swarm Algorithm		
MR	Magnetic Resonance		
MC	Marching Cube		
MK	Markedness		
LR	Low Resolution		
SVM	Support Vector Machine		
MDC	Max Distance Constraint		

Disclosure statement

No potential conflict of interest was reported by the author(s).

Notes on contributors

Aju Dennisan is currently working as an Associate Professor in Vellore Institute of Technology with 17 years of teaching and research experience. He is an eminent person with research interest in image processing, medical imaging, multimedia systems and computer graphics. He has numerous research article publications in peer-reviewed journals under his authorship.

Sushitha Susan Joseph is a Research Scholar in VIT, Vellore with 6 years of teaching experience. Her research interest include medical image processing and she is working on various tumor related topics.

References

- file:///E:/2021/03%20March%202021/Sushana%20107615%20-%20Paper%202/hist_eq.pdf <https://www.kdnuggets.com/2019/08/introduction-image-segmentation-k-means-clustering.html>
- Afzal AMS. 2021. Optimized support vector machine model for visual sentiment analysis. In: 2021 3rd International Conference on Signal Processing and Communication (ICPSC). IEEE. p. 171–175.
- Agus M, Boges D, Calí C. 2018. GLAM: glycogen-derived lactate absorption map for visual analysis of dense and sparse surface reconstructions of rodent brain structures on desktop systems and virtual environments. Comput Graphics. 74:85–98. (Cover date: August 2018). doi:[10.1016/j.cag.2018.04.007](https://doi.org/10.1016/j.cag.2018.04.007).
- Agus M, Castillo MV, Calí C. 2019. Shape analysis of 3D nanoscale reconstructions of brain cell nuclear envelopes by implicit and explicit parametric representations. Comput Graphics: X. 1:Art. no.100004. (Cover date: June 2019).
- Akbary P, Ghiasi M, Pourkheranjani MRR, Alipour H, Ghadimi N. 2019. Extracting appropriate nodal marginal prices for all types of committed reserve. Comput Econ. 53(1):1–26. doi:[10.1007/s10614-017-9716-2](https://doi.org/10.1007/s10614-017-9716-2).
- Bisandu DB, Moulitsas I, Filippone S. 2022. Social ski driver conditional autoregressive-based deep learning classifier for flight delay prediction. Neural Comput Appl. 34(11):1–26.
- Bollero P, Rocco F, Gianfreda F, Gualtieri P, Miranda M, Barlattani A. 2019. Epidemiology, etiopathogenesis, treatment and prognosis of oral thermal burns from food and drinks. Dent Hypotheses. 10(3):80–81. doi:[10.4103/denthyp.denthyp_56_19](https://doi.org/10.4103/denthyp.denthyp_56_19).
- Chandanapalli SB, Reddy ES, Lakshmi DR. 2019. Convolutional neural network for water quality prediction in WSN. J Commun Netw. 2(3):40–47.
- Cingireddy AR, Ghosh R, Melapu VK, Joginipelli S, Kwembe TA. 2022. Classification of Parkinson's disease using motor and non-motor biomarkers

- through machine learning techniques. *Int J Quant Struct Prop Relatsh.* 7(2):1–21. doi:[10.4018/IJQSPR.2900011](https://doi.org/10.4018/IJQSPR.2900011).
- Cronin MJ, Xu J, Dortch RD. 2020. Rapid whole-brain quantitative magnetization transfer imaging using 3D selective inversion recovery sequences. *Magn Reson Imaging.* 68:66–74. (Cover date: May 2020). doi:[10.1016/j.mri.2020.01.014](https://doi.org/10.1016/j.mri.2020.01.014).
- Dehghani M, Ghiasi M, Niknam T, Kavousi-Fard A, Shasadeghi M, Ghadimi N, Taghizadeh-Hesary F. 2020. Blockchain-Based securing of data exchange in a power transmission system considering congestion management and social welfare. *Sustainability.* 13(1):90. doi:[10.3390/su13010090](https://doi.org/10.3390/su13010090).
- Duc TN, Quan TM, Jeong WK. 2019. Frequency-Splitting dynamic MRI reconstruction using multi-scale 3D convolutional sparse coding and automatic parameter selection. *Med Image Anal.* 53:179–196. (Cover date: April 2019). doi:[10.1016/j.media.2019.02.001](https://doi.org/10.1016/j.media.2019.02.001).
- Du J, He Z, Jia Y. 2019. Super-Resolution reconstruction of single anisotropic 3D MR images using residual convolutional neural network. *Neurocomputing.* 392:209–220. (Cover date: 7 June 2020). doi:[10.1016/j.neucom.2018.10.102](https://doi.org/10.1016/j.neucom.2018.10.102).
- Du J, Wang L, Liu Y, Zhou Z, He Z, Jia Y. 2020. Brain MRI super-resolution using 3D dilated convolutional encoder–Decoder network. *IEEE Access.* 8:18938–18950. doi:[10.1109/ACCESS.2020.2968395](https://doi.org/10.1109/ACCESS.2020.2968395).
- Ebner M, Wang G, Vercauteren T. 2019. An automated framework for localization, segmentation and super-resolution reconstruction of fetal brain MR. *NeuroImage.* 206:Art. no. 116324. (Cover date: 1 February 2020). doi:[10.1016/j.neuroimage.2019.116324](https://doi.org/10.1016/j.neuroimage.2019.116324).
- Fang L, Wang Z, Chen Z, Jian F, Li S, He H. 2020. 3D shape reconstruction of lumbar vertebra from two X-ray images, a CT model. *IEEE/CAA J Autom Sin.* 7(4):1124–1133. doi:[10.1109/JAS.2019.1911528](https://doi.org/10.1109/JAS.2019.1911528).
- Franco R, Gianfreda F, Miranda M, Barlattani A, Bollero P. 2020. The hemostatic properties of chitosan in oral surgery. *Biomed Biotechnol Res J.* 4 (3):186. doi:[10.4103/bbrj.bbrj_43_20](https://doi.org/10.4103/bbrj.bbrj_43_20).
- Fujita S, Hagiwara A, Aoki S. 2019. Three-Dimensional high-resolution simultaneous quantitative mapping of the whole brain with 3D-QALAS: An accuracy and repeatability study. *Magn Reson Imaging.* 63:235–243. (Cover date: November 2019). doi:[10.1016/j.mri.2019.08.031](https://doi.org/10.1016/j.mri.2019.08.031).
- Gangappa M, Mai CK, Sammular P. 2019. Enhanced crow search optimization algorithm and hybrid NN-CNN classifiers for classification of land cover images. *Multimed Syst.* 2(3):12–22.
- George A, Rajakumar BR. 2013. APOGA: an adaptive population pool size based genetic algorithm. *AASRI Procedia - 2013 AASRI Conf Intell Syst Control (ISC 2013).* 4:288–296. doi:[10.1016/j.aasri](https://doi.org/10.1016/j.aasri).
- Germanò E, Gagliano A, Arena C, Cedro C, Vetri L, Operto FF, Pastorino GMG, Marotta R, Roccella M. 2020. Reading–writing disorder in children with idiopathic epilepsy. *Epilepsy Behav.* 111:107118. doi:[10.1016/j.yebeh.2020.107118](https://doi.org/10.1016/j.yebeh.2020.107118).
- Ghadimi N, Akbarimajd A, Shayeghi H, Abedinia O. 2018. Two stage forecast engine with feature selection technique and improved meta-heuristic algorithm for electricity load forecasting. *Energy.* 161:130–142. doi:[10.1016/j.energy.2018.07.088](https://doi.org/10.1016/j.energy.2018.07.088).
- Ghosh R, Cingreddy AR, Melapu V, Joginipelli S, Kar S. 2021. Application of artificial intelligence and machine learning techniques in classifying extent of dementia across Alzheimer’s image data. *Int J Quant Struct Prop Relatsh.* 6(2):29–46. doi:[10.4018/IJQSPR.2021040103](https://doi.org/10.4018/IJQSPR.2021040103).
- Gokulkumari G. 2020. Classification of brain tumor using manta ray foraging optimization-based DeepCNN classifier. *Multimed Syst.* 3(4):32–42. doi:[10.46253/j.mr.v3i4.a4](https://doi.org/10.46253/j.mr.v3i4.a4).
- Gopal A. 2020. Hybrid classifier: brain tumor classification and segmentation using genetic-based grey wolf optimization. *Multimed Syst.* 3(2):1–10.
- Han X, Kwitt R, Niethammer M. 2018. Brain extraction from normal and pathological images: a joint PCA/Image-reconstruction approach. *NeuroImage.* 176:431–445. (Cover date: 1 August 2018). doi:[10.1016/j.neuroimage.2018.04.073](https://doi.org/10.1016/j.neuroimage.2018.04.073).
- Hu HH, Benkert T, Block KT. 2019. 3D T1-weighted contrast-enhanced brain MRI in children using a fat-suppressed golden angle radial acquisition: an alternative to Cartesian inversion-recovery imaging. *Clin Imaging.* 55:112–118. (Cover date: May–June 2019). doi:[10.1016/j.clinimag.2019.02.006](https://doi.org/10.1016/j.clinimag.2019.02.006).
- Jang MY, Park CR, Lee Y. 2020. Experimental study of the fast non-local means noise reduction algorithm using the Hoffman 3D brain phantom in nuclear medicine SPECT image. *Optik.* 224:Art. no. 165440. (Cover date: December 2020).
- Joseph S. S. 2021. Three dimensional reconstruction of brain tumors from 2D MRI scans: optimized curve fitting process. *communication.*
- Jurek J, Kociński M, Majos A. 2019. CNN-Based super resolution reconstruction of 3D MR images using thick-slice scans. *Biocybern Biomed Eng.* 40 (1):111–125. (Cover date: January–March 2020). doi:[10.1016/j.bbce.2019.10.003](https://doi.org/10.1016/j.bbce.2019.10.003).
- Kaur S, Awasthi LK, Sangal AL, Dhiman G. 2020. Tunicate swarm algorithm: a new bio-inspired based metaheuristic paradigm for global optimization. *Eng Appl Artif Intell.* 90:103541. doi:[10.1016/j.engappai.2020.103541](https://doi.org/10.1016/j.engappai.2020.103541).
- Khodaei H, Hajiali M, Darvishan A, Sepehr M, Ghadimi N. 2018. Fuzzy-Based heat and power hub models for cost-emission operation of an industrial consumer using compromise programming. *Appl Therm Eng.* 137:395–405. doi:[10.1016/j.applthermaleng.2018.04.008](https://doi.org/10.1016/j.applthermaleng.2018.04.008).
- Kumhar SH, Kirmani MM, Sheetlani J, Hassan M. 2020. Sentiment analysis of Urdu language on different social media platforms using word2vec and LSTM. *Turkish J Comput Math Educ (TURCOMAT).* 11 (3):1439–1447.
- Lakhekar GV, Roy RG. 2014. A fuzzy neural approach for dynamic spectrum allocation in cognitive radio networks. In: 2014 International Conference on Circuits, Power and Computing Technologies [ICCPCT-2014], Nagercoil, India. IEEE. p. 1455–1461.
- LeCun Y, Kavukcuoglu K, Farabet C. 2010. Convolutional networks and applications in vision. In: Circuits and Systems, International Symposium on, Nagercoil, India. p. 253–256.
- Lu W, Song Z, Chu J. 2020. A novel 3D medical image super-resolution method based on densely connected network. *Biomed Signal Process Control.* 62:Art. no. 102120. (Cover date: September 2020). doi:[10.1016/j.bspc.2020.102120](https://doi.org/10.1016/j.bspc.2020.102120).
- Mehmood I, Sajjad M, Muhammad K, Shah SIA, Sangaiah AK, Shoaib M, Baik SW. 2019. An efficient computerized decision support system for the analysis and 3D visualization of brain tumor. *Multimed Tools Appl.* 78:12723–12748. doi:[10.1007/s11042-018-6027-0](https://doi.org/10.1007/s11042-018-6027-0).
- Mirjalili S, Mirjalili SM, Lewis A. 2014. Grey Wolf optimizer. *Adv Eng Softw.* 69:46–61. doi:[10.1016/j.advengsoft.2013.12.007](https://doi.org/10.1016/j.advengsoft.2013.12.007).
- Mzoughi H, Njeh I, Wali A, Slima MB, BenHamida A, Mhiri C, Mahfoudhe KB. 2020. Deep multi-scale 3D convolutional neural network (CNN) for MRI gliomas brain tumor classification. *J Digit Imaging.* 33:903–915. doi:[10.1007/s10278-020-00347-9](https://doi.org/10.1007/s10278-020-00347-9).
- Parsian A, Ramezani M, Ghadimi N. 2017. A hybrid neural network-gray wolf optimization algorithm for melanoma detection. *Biomed Res.* 28 (8):3408–3411.
- Petersen MV, Mlakar J, McIntyre. 2019. Holographic reconstruction of axonal pathways in the human brain. *Neuron.* 104(6):1056–1064.e3. (Cover date: 18 December 2019). doi:[10.1016/j.neuron.2019.09.030](https://doi.org/10.1016/j.neuron.2019.09.030).
- Precenzano F, Parisi, L, Lanza, V, Vetrici, L, Operto, F.F, Pastorino, G.M.G, Ruberto, M, Messina, G, Risoleo, M.C, Santoro, C, et al. 2020. Electroencephalographic abnormalities in autism spectrum disorder: Characteristics and therapeutic implications. *Medicina.* 56(9):419. doi:[10.3390/medicina56090419](https://doi.org/10.3390/medicina56090419).
- Rajakumar BR. 2013a. Impact of static and adaptive mutation techniques on genetic algorithm. *Int J Hybrid Intell Syst.* 10(1):11–22. doi:[10.3233/HIS-120161](https://doi.org/10.3233/HIS-120161).
- Rajakumar BR. 2013b. Static and adaptive mutation techniques for genetic algorithm: a systematic comparative analysis. *Int J Comput Sci Eng.* 8 (2):180–193. doi:[10.1504/IJCSE.2013.053087](https://doi.org/10.1504/IJCSE.2013.053087).
- Rajakumar BR, George A. 2012. A new adaptive mutation technique for genetic algorithm. In: proceedings of IEEE International Conference on Computational Intelligence and Computing Research (ICCIC); Coimbatore (India). p. 1–7. DOI: [10.1109/ICCIC.2012.6510293](https://doi.org/10.1109/ICCIC.2012.6510293).
- Rao TCS, Ram SST, Subrahmanyam JBV. 2019. Enhanced deep convolutional neural network for fault signal recognition in the power distribution system. *J Comput Mech Power Syst Control.* 2(3):39–46.
- Rathod S. 2020. Hybrid metaheuristic algorithm for cluster head selection in WSN. *J Commun Netw.* 3(4):101504.
- Razmjooy N, Ramezani M, Ghadimi N. 2017. Imperialist competitive algorithm-based optimization of neuro-fuzzy system parameters for automatic red-

- eye removal. *Int J Fuzzy Syst.* 19(4):1144–1156. doi:[10.1007/s40815-017-0305-2](https://doi.org/10.1007/s40815-017-0305-2).
- Razmjooy N, Sheykhamad FR, Ghadimi N. 2018. A hybrid neural network-world cup optimization algorithm for melanoma detection. *Open Med.* 13(1):9–16. doi:[10.1515/med-2018-0002](https://doi.org/10.1515/med-2018-0002).
- Rustam F, Khalid M, Aslam W, Rupapara V, Mehmmood A, Choi GS. 2021. A performance comparison of supervised machine learning models for Covid-19 tweets sentiment analysis. *PLoS One.* 16(2):e0245909. doi:[10.1371/journal.pone.0245909](https://doi.org/10.1371/journal.pone.0245909).
- Sadiq S, Umer M, Ullah S, Mirjalili S, Rupapara V, Nappi M. 2021. Discrepancy detection between actual user reviews and numeric ratings of google app store using deep learning. *Expert Syst Appl.* 181:115111. doi:[10.1016/j.eswa.2021.115111](https://doi.org/10.1016/j.eswa.2021.115111).
- Saeedi M, Moradi M, Hosseini M, Emamifar A, Ghadimi N. 2019. Robust optimization based optimal chiller loading under cooling demand uncertainty. *Appl Therm Eng.* 148:1081–1091. doi:[10.1016/j.applthermeng.2018.11.122](https://doi.org/10.1016/j.applthermeng.2018.11.122).
- Sai Ambati L, Narukonda K, Bojja GR, Bishop D. 2020. Factors influencing the adoption of artificial intelligence in organizations-from an employee's perspective.
- Shaik JB, Ganesh V. 2020. Deep neural network and social ski-driver optimization algorithm for power system restoration with VSC - HVDC technology. *J Comput Mech Power Syst Control.* 3(1):1–9.
- Sharma S. 2020. Self supervised methods towards human activity recognition. *IOSR J Comput Eng (IOSR-JCE).* 22(6):51–56.
- Shaul R, David I, Shirit O, Raviv T.R. 2020. Subsampled brain MRI reconstruction by generative adversarial neural networks. *Med Image Anal.* 65:101747. doi:[10.1016/j.media.2020.101747](https://doi.org/10.1016/j.media.2020.101747).
- Sumathi R, Venkatesulu M, Arjuna SP. 2018. Extracting tumor in MR brain and breast image with Kapur's entropy based cuckoo search optimization and morphological reconstruction filters. *Biocybern Biomed Eng.* 38(4):918–930. (Cover date: 2018). doi:[10.1016/j.bbce.2018.07.005](https://doi.org/10.1016/j.bbce.2018.07.005).
- Swamy SM, Rajakumar BR, Valarmathi IR. 2013. Design of hybrid wind and photovoltaic power system using opposition-based genetic algorithm with Cauchy mutation. In: IET Chennai Fourth International Conference on Sustainable Energy and Intelligent Systems (SEISCON 2013); Chennai (India). doi: [10.1049/ic.2013.0361](https://doi.org/10.1049/ic.2013.0361)
- Tang Y. 2016. Vehicle tracking and counting based on vehicle recognition. *China Comput Commun J.* 13:97–98.
- Umaba R, Uda T, Ohata K. 2018. Anatomic understanding of posterior quadrant disconnection from cadaveric brain, 3D reconstruction and simulation model, and intraoperative photographs. *World Neurosurg.* 120:e792–e801. (Cover date: December 2018). doi:[10.1016/j.wneu.2018.08.168](https://doi.org/10.1016/j.wneu.2018.08.168).
- Vinolin V, Vinusha S. 2018. Enhancement in biodiesel blend with the aid of neural network and SAPSO. *J Comput Mech Power Syst Control.* 1(1):11–17.
- Wang Wang G.G, Deb S, Leandro, C. 2015. Elephant herding optimization. doi:[10.1109/ISCBI.2015.8](https://doi.org/10.1109/ISCBI.2015.8).
- Wei H, Cao S, Liu C. 2019. Learning-Based single-step quantitative susceptibility mapping reconstruction without brain extraction. *NeuroImage.* 202:Art. no. 116064. (Cover date: 15 November 2019). doi:[10.1016/j.neuroimage.2019.116064](https://doi.org/10.1016/j.neuroimage.2019.116064).
- Xu Z, Sheykhamad FR, Ghadimi N, Razmjooy N. 2020. Computer-Aided diagnosis of skin cancer based on soft computing techniques. *Open Med.* 15(1):860–871. doi:[10.1515/med-2020-0131](https://doi.org/10.1515/med-2020-0131).
- Xu Z, Xiao C, Xu X. 2010. An improved marching cubes algorithm based on edge contraction. In: IEEE 10th International conference on signal processing proceedings; Beijing (China). p. 944–947. doi: [10.1109/ICOSP.2010.5655719](https://doi.org/10.1109/ICOSP.2010.5655719).
- Zhang Y, Yap PT, Shen D. 2019. Super-Resolution reconstruction of neonatal brain magnetic resonance images via residual structured sparse representation. *Med Image Anal.* 55:76–87. (Cover date: July 2019). doi:[10.1016/j.media.2019.04.010](https://doi.org/10.1016/j.media.2019.04.010).
- Zheng H, Yao L, Chen M, Long Z. 2020. 3D contrast image reconstruction from human brain activity. *IEEE Trans Neural Syst Rehabil Eng.* 28 (12):2699–2710. doi:[10.1109/TNSRE.2020.3035818](https://doi.org/10.1109/TNSRE.2020.3035818).
- Zhou Z, He Z, Chen D. 2020a. 3D dense connectivity network with atrous convolutional feature pyramid for brain tumor segmentation in magnetic resonance imaging of human heads. *Comput Biol Med.* 121:Art. no. 103766. (Cover date: June 2020). doi:[10.1016/j.combiomed.2020.103766](https://doi.org/10.1016/j.combiomed.2020.103766).
- Zhou Z, He Z, Jia Y. 2020b. Afpnet: a 3D fully convolutional neural network with atrous-convolution feature pyramid for brain tumor segmentation via MRI images. *Neurocomputing.* 402:235–244. (Cover date: 18 August 2020). doi:[10.1016/j.neucom.2020.03.097](https://doi.org/10.1016/j.neucom.2020.03.097).